Article
journal of Studies of Earth's Deep Interior
doi:10.46298/jsedi.17268

Principal component analysis of the 2010 reversal of core-surface flow beneath the Pacific Ocean

Frederik Dahl Madsen * [1,2,3], **Isobel Howard** [1,3], **William J. Brown** [2], **Kathryn A. Whaler** [1,3]

[1]School of GeoSciences, University of Edinburgh, Edinburgh, United Kingdom, [2]British Geological Survey, Lyell Centre, Edinburgh, United Kingdom, [3]Edinburgh Centre for Planetary Science, University of Edinburgh, Edinburgh, United Kingdom

Author contributions: *Conceptualization*: Frederik Dahl Madsen, William Brown, Kathryn A. Whaler. *Methodology*: Frederik Dahl Madsen, Isobel Howard, William Brown, Kathryn A. Whaler. *Formal Analysis*: Frederik Dahl Madsen, Isobel Howard. *Investigation*: Frederik Dahl Madsen, Isobel Howard. *Writing - Original draft*: Frederik Dahl Madsen. *Writing - Review & Editing*: Frederik Dahl Madsen, Isobel Howard, William J. Brown, Kathryn A. Whaler. *Supervision*: Frederik Dahl Madsen, William J. Brown, Kathryn A. Whaler. *Funding acquisition*: Frederik Dahl Madsen, William J. Brown, Kathryn A. Whaler.

Abstract Outer core surface flow is predominantly westward, with historically slow flow in the Pacific. However, core surface flow models since 2011 have relatively strong eastward flow in the equatorial Pacific. We invert geomagnetic secular variation data from ground and satellite observations, from 1997 to 2025, to obtain a time-dependent model of core-surface flow. By decomposing the flow into its principal components, we find that ~95% of the flow variance is described by the relatively steady eccentric planetary gyre and high-latitude jet. The second principal component of the flow, which explains another ~4% of the flow variance, shows the flow beneath the equatorial Pacific turning in 2010 from weakly westward to strongly eastward. Our models suggest that the Pacific eastward flow has been weakening again since 2020. The remaining ~1% of the flow variance accounts for standing and propagating waves at the core surface. We propose that the reversal of the Pacific flow is related to events in the deeper core around 2010, evidenced by seismological and geodetic studies.

Handling Editor: Chris Davies
Received: January 9, 2026
Revised: April 1, 2026; April 14, 2026
Accepted: April 20, 2026
Published: May 6, 2026

Non-technical summary The flow of the liquid iron alloy in the Earth's outer core generates the geomagnetic field and its rate of change, the secular variation (SV). On timescales shorter than centuries, we can invert SV observations from ground observatories and geomagnetic satellites for models of the fluid flow at the top of the core, assuming the magnetic field is "frozen" into the liquid. We perform principal component analysis of the core-surface flow, derived from observations of SV from 1997 to 2025. Historically, the core-surface flow has been predominantly westward, as required to maintain a westward-drifting magnetic field. This westward flow is a component of an eccentric planetary gyre, offset from the Earth's rotation axis. The flow in the equatorial Pacific is not part of this gyre, and we find that it changed in 2010 from weakly westward to strongly eastward. Our model suggests that the Pacific eastward flow has been weakening since 2020. The rise of the strong eastward flow in the Pacific is contemporary with a change in behaviour in the inner core, as inferred from geodesy and seismology, and we hypothesise that these changes in the deep interior are associated with the changes in flow beneath the Pacific.

1 Introduction

The Earth's magnetic field is generated by complex motions of a liquid iron mixture in the outer core. Through dynamo action, the magnetic field is constantly changing as a result of this dynamic and complex system (e.g. Gubbins and Roberts, 1987). On timescales of months to decades, the rate of change of the magnetic field, also known as secular variation (SV), is often considered as being dominated by advective flow at the core surface (e.g. Holme, 2015). We can therefore use observations of SV to infer information about the flow structures in the core. Traditionally, the large-scale core surface flow has been considered to be predominantly westward, associated with the so-called westward drift of the magnetic field (e.g. Jackson et al., 2000), and recent inversions of palaeomagnetic field models have suggested that this westward drift has persisted over the past 9000 years (Suttie et al., 2025).

The westward flow is a component of the eccentric planetary gyre (e.g. Pais and Jault, 2008; Finlay et al., 2023), which concentrates the flow beneath the equatorial Atlantic, and towards the tangent cylinder in the Pacific hemisphere. The flow beneath the equatorial Pacific, unaffected by the gyre, was weakly westward until the turn of the 2010s (e.g. Holme, 2015; Istas et al., 2023), and it changed to strongly eastward after 2012 (Whaler et al., 2022; Ropp and Lesur, 2023; Rogers et al., 2025; Grüne et al., 2025). This precedes the onset of significant geomagnetic jerk activity, (defined as abrupt changes in SV, e.g. Courtillot et al., 1978; Brown et al., 2013), in the Pacific region, starting in 2017 (see Whaler et al. (2022),

*Corresponding author: f.d.madsen@sms.ed.ac.uk

Pavón-Carrasco et al. (2021), and Madsen et al. (2026) for explicit investigations of the 2017, 2020, and 2024 jerks, respectively), disruption to periodic signals in the length-of-day (ΔLOD, Madsen and Holme, 2025; Howard et al., 2025), and seismic signatures of changes to the inner core (e.g. Yang and Song, 2023; Vidale et al., 2025).

Recent efforts to investigate contemporary core dynamics have utilised geomagnetic virtual observatories (GVOs, Mandea and Olsen, 2006), derived from high-resolution satellite data. Low-Earth orbiting satellite missions like Ørsted (1999–2005, e.g. Neubert et al., 2001), CHAMP (2000–2010, e.g. Reigber, 2004) and Swarm (2013–ongoing, e.g. Friis-Christensen et al., 2006) have provided near-global coverage of the Earth's magnetic field since 1999 (e.g. Grüne et al., 2025; Claveau et al., 2025; Kloss et al., 2026), with only an unfortunate gap from 2010 to 2013 – exactly when the flow underneath the Pacific reversed direction. Although magnetic measurements suitable for geomagnetic modelling are available from platform magnetometers on other missions such as CryoSat-2 (2011–ongoing, Hammer, Finlay, et al., 2021), it is necessary to complement the satellite data during the gap between dedicated magnetometry missions with long-running ground observatory (GO) data.

In this article, we utilise recent high-resolution geomagnetic satellite and ground observatory data to investigate the dynamics of the recent changes to Pacific core surface flow, and its impact on the observed SV. We do this by employing principal component analysis (PCA) on models of the core-surface flow covering the period 1997.67–2025.00 obtained with three different assumptions about the flow. We first summarise our flow-modelling strategies, and outline the PCA method employed on the flow models in Section 2. We then present our flow models, and their decomposition into principal components in Section 3. We discuss the implications of the 2010 Pacific overturn on core dynamics and geomagnetic field modelling in Section 4 and conclude in Section 5.

2 Data and Methods

We generated an updated model of core-surface flow following the work of Grüne et al. (2025), who created a continuous, time-dependent core-surface flow model from G(V)O data, spanning 1997.67–2023. In order to further investigate the spatiotemporal flow changes in the Pacific, we expand the model with the additional frameworks developed by Whaler et al. (2016) on temporal constraints on zonal flow and Madsen et al. (2025) on limiting equatorially asymmetric flow. The methodology used to derive these flows, along with the data used in this study, are summarised here.

2.1 Data

Our dataset contains 4-monthly mean vector SV data from GOs (1997.67–2023.33), as well as GVOs created from Ørsted (1999.67–2005.00), CHAMP (2001.00–2009.67), CryoSat-2 (2011.00–2018.00) and Swarm (2014.67–2025.00). Data contributing to the GVOs are all processed following the methodology of Hammer, Cox, et al. (2021). The GVO dataset from each satellite comprises three-component vector time series of the magnetic field, as observed on a regularly spaced grid of 300 locations on the Earth, at constant altitude, representative of the corresponding satellite orbit. The GO data are compiled from hourly mean values (Macmillan and Olsen, 2013). Data for both GOs and GVOs are chosen during geomagnetically quiet night-time, and then cleaned of external field contamination as described (for GOs only) by Olsen et al. (2014). SV is obtained from annual differences of these data, and their associated errors are computed from the residuals between the G(V)O datum and the estimate of the CHAOS-8.3 core field model at the location of observation. The temporal distribution of the data is shown in Figure 1.

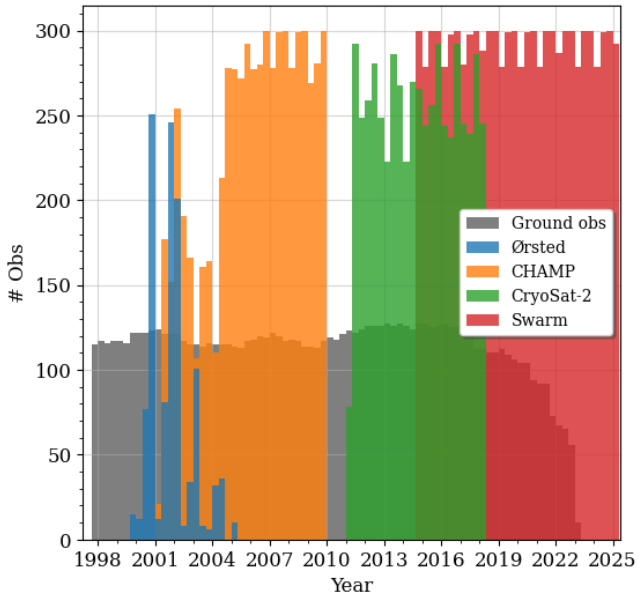

Figure 1: Number of G(V)Os within each 4-month bin

2.2 Core-surface flow models

The reduced induction equation describes the relationship between the horizontal flow, $\mathbf{u}_\mathrm{H}$, and the radial magnetic field, B_r, at the surface of the core:

$$\dot{B}_r = -\nabla_\mathrm{H} \cdot (\mathbf{u}_\mathrm{H} B_r). \tag{1}$$

Here, the overdot indicates the partial time derivative, and the subscript $\mathbf{H}$ indicates the horizontal components of a given vector, all represented in spherical polar coordinates. This is assuming negligible magnetic diffusion (e.g. Roberts and Scott, 1965). Although we note that recent numerical dynamo simulations suggest that diffusion may be important in boundary layers adjacent to the core-mantle boundary (CMB, Tsang and Jones, 2024), Jault et al. (2026) found that the relative importance of advection versus diffusion there is not governed by the magnetic Reynolds number (a non-dimensional number describing the dominance of magnetic advection versus diffusion), but rather by the local value of the Elsasser number (a non-dimensional number describing the dominance of magnetic forces to rotational forces). In the Earth, the Elsasser number is likely large enough for diffusion to be subdominant at the CMB, and the frozen flux assumption therefore remains an acceptable approximation. If we further assume that the mantle is electrically insulating, we can express the magnetic field originating in the core as the gradient of a potential field, V,

$$\mathbf{B}(r,\theta,\phi) = -\nabla V(r,\theta,\phi) \tag{2}$$

which in turn can be represented in terms of spherical harmonics:

$$V(r,\theta,\phi,t) = a\sum_{l=1}^{L_B}\sum_{m=0}^{l}\left(\frac{a}{r}\right)^{l+1}\left(g_l^m(t)\cos m\phi + h_l^m(t)\sin m\phi\right)P_l^m(\cos\theta), \tag{3}$$

where a is the reference radius, normally taken to be the mean radius of the Earth, l and m are the spherical harmonic degree and order, L_B is the maximum spherical harmonic degree we evaluate the magnetic field to (usually $L_B = 14$ due to Earth's magnetised crust, e.g. Cain et al., 1989), g_l^m and h_l^m are the spherical harmonic weights, referred to as Gauss coefficients, and $P_l^m(\cos\theta)$ are the Schmidt quasi-normalised associated Legendre functions. Similarly, the flow can be expressed in a spherical harmonic basis, if we decompose it into its toroidal and poloidal components (e.g. Roberts and Scott, 1965). This is only possible under the assumption that the flow is incompressible, such that $\nabla\cdot\mathbf{u} = 0$ (e.g. Gubbins and Roberts, 1987; Holme, 2015). At the CMB where $u_r = 0$, the flow can be expressed as

$$\mathbf{u_H} = \nabla\times(\mathcal{T}\mathbf{r}) + \nabla_\mathbf{H}(\mathcal{S}\mathbf{r}), \tag{4}$$

where $\mathcal{T}$ and $\mathcal{S}$ are the toroidal and poloidal flow scalar potentials, respectively (e.g. Gubbins and Roberts, 1987; Holme, 2015). We can thus express $\mathcal{T}$ and $\mathcal{S}$ as a sum of spherical harmonics:

$$\mathcal{T}(\theta,\phi,t) = \sum_{l=1}^{L_u}\sum_{m=0}^{l}(t_l^{m\,c}(t)\cos m\phi + t_l^{m\,s}(t)\sin m\phi)P_l^m(\cos\theta), \tag{5}$$

$$\mathcal{S}(\theta,\phi,t) = \sum_{l=1}^{L_u}\sum_{m=0}^{l}(s_l^{m\,c}(t)\cos m\phi + s_l^{m\,s}(t)\sin m\phi)P_l^m(\cos\theta).$$

Here, $t_l^{m\,c,s}$ and $s_l^{m\,c,s}$ are the spherical harmonic coefficients for toroidal and poloidal flow, respectively. We truncate the series at spherical harmonic degree L_u.

With these relations in mind, we can re-express equation (1) in matrix notation. Substituting equations (3) and (5) into equation (1), we obtain the expression

$$\mathbf{d} = \mathbf{A}\mathbf{m}, \tag{6}$$

where $\mathbf{d}$ is a vector that contains SV data, the vector $\mathbf{m}$ contains the toroidal and poloidal flow coefficients, and $\mathbf{A}$ is the equations of condition matrix, which relates the two vectors. $\mathbf{A}$ depends on a model of the CMB magnetic field (Whaler, 1986; Beggan and Whaler, 2008; Grüne et al., 2025) — we use the CHAOS-8.3 model (Kloss et al., 2026).

We invert equation (6), imposing spatial and temporal regularisation schemes to reduce the inherent non-uniqueness in this problem (e.g. Holme, 2015). Spatially, we make the assumption that the flow is large scale, (i.e. all the flow energy is contained within flow coefficients of degrees $l \le L_u$). Furthermore, we impose the so-called 'strong norm' of Bloxham (1988) to penalise the small scale flow by minimising the second derivatives of flow over the core surface,

$$\oint_\Omega \left(\left(\nabla^2_\mathbf{H}u_\theta\right)^2 + \left(\nabla^2_\mathbf{H}u_\phi\right)^2\right)\mathrm{d}\Omega, \tag{7}$$

where Ω is the CMB. The temporal regularisation is chosen to minimise the difference in flow between successive epochs (Whaler et al., 2016). We therefore invert all the data simultaneously for a time-dependent flow. The regularised least-squares solution to equation (6) thus takes the form

$$\hat{\mathbf{m}} = (\mathbf{A}^\mathrm{T}{\mathbf{C_e}}^{-1}\mathbf{A} + \lambda_v{\mathbf{C_m}}^{-1} + \lambda_t\mathbf{D}^\mathrm{T}\mathbf{D})^{-1}\mathbf{A}^\mathrm{T}{\mathbf{C_e}}^{-1}\mathbf{d}, \tag{8}$$

where $\mathbf{C_e}$ is the data covariance matrix, which consists of the variances for each datum at each G(V)O arranged along the diagonal, respectively, and zeroes elsewhere. $\mathbf{C_m}$ is the *a priori* model covariance matrix (implementing the strong norm), $\mathbf{D}$ is the temporal first differences matrix (explicitly given by Whaler et al., 2016), and λ_v and λ_t are the spatial and temporal damping factors, respectively. We refer to a flow obtained from this procedure as a minimum acceleration model.

From this model, we create two additional types of flow models, similar to those of Madsen et al. (2025). The first allows zonal variations to dominate the temporal variations of the flow. Whaler et al. (2016) removed the temporal damping on odd-degree zonal toroidal flow coefficients, allowing for fast rigid zonal flows, such as associated with fast torsional oscillations (e.g. Teed et al., 2019). They found that the resulting flow could better reproduce ΔLOD observations. Therefore, following their methodology, we relax (rather than remove) the temporal damping on the odd degree, zonal toroidal coefficients in this model, yielding two temporal damping parameters, λ_t^{zt} and λ_t^{nzt}, where λ_t^{zt} damps the odd-degree, zonal toroidal coefficients and λ_t^{nzt} damps all other flow coefficients. These damping parameters act on different elements of the temporal damping matrix, $\mathbf{D}^\mathbf{T}\mathbf{D}$. Here, the choice of λ_t^{zt} and λ_t^{nzt} are the same as those used by Madsen et al. (2025), where the values were chosen to obtain the best fit to ΔLOD observations, while still yielding a comparable root-mean-squared (rms) data misfit as for our minimum acceleration model. Here, the spatial damping is applied to all flow coefficients with the same damping parameter as for the minimum acceleration model. This flow will be referred to as the TO-like flow.

The second type of model investigates the level of equatorial asymmetry required to fit the data during the flow reversal in the Pacific, by spatially damping the equatorially symmetric and antisymmetric flow coefficients differently, thus yielding two spatial damping parameters; $\lambda_v^{\mathrm{asymm}}$ and $\lambda_v^{\mathrm{symm}}$, which act on different elements of the matrix $\mathbf{C_m}$. We choose similar values of $\lambda_v^{\mathrm{asymm}}$ and $\lambda_v^{\mathrm{symm}}$ to Madsen et al. (2025), aiming to obtain minimal equatorial antisymmetry, while keeping a comparable model rms data misfit as for our minimum acceleration models and retaining a similar amount of spatial complexity. In this model, the temporal damping is the same on all flow parameters. We refer to this as the symmetric-asymmetric flow, or SA flow.

2.3 Principal component analysis of flow coefficients

The following section uses nomenclature similar to that of Pais et al. (2015), but whereas they undertook their PCA decomposition on a regular grid of values on a sphere, we complete the PCA on the flow in spectral space, combined for the toroidal and poloidal flow coefficients, but independently for each flow type.

After obtaining our flow model expressed in spherical harmonic coefficients, we compile the spatiotemporal informa-

tion into a matrix, $\mathbf{X}$:

$$\mathbf{X} = \begin{bmatrix} x_{11} & x_{12} & \dots & x_{1N_u} \\ x_{21} & x_{22} & \dots & x_{2N_u} \\ \vdots & \vdots & \ddots & \vdots \\ x_{N_t} & x_{N_t} & \dots & x_{N_tN_u} \end{bmatrix}, \tag{9}$$

where x_{ij} represents the flow coefficient j at timestep i, $N_u = 2L_u(L_u+2)$ is the maximum number of flow coefficients, N_t is the number of epochs of data, and flow coefficients are given in the traditional order as $\mathbf{x}_i = [x_1^{0\,c}, x_1^{1\,c}, x_1^{1\,s}, x_2^{0\,c}, \dots x_{L_u}^{L_u\,c}, x_{L_u}^{L_u\,s}]_i$, with toroidal flow coefficients presented first, followed by the poloidal. In other words, $\mathbf{X}$ contains rows of snapshots of flow coefficients, and columns of time-series for each flow coefficient. Where some studies employing PCA require the columns of $\mathbf{X}$ to be standardised and normalised (e.g. Jolliffe, 2002), we reject this step similarly to Pais et al. (2015), as the comparative amplitude of the flow coefficients have a physical meaning, and normalising them would disproportionally enhance smaller scale signals. We experimented with normalising the flow coefficients by their associated kinetic energy (e.g. Gillet et al., 2019), and found this to make little difference (See Supplementary Figure S2.1).

The covariance matrix for $\mathbf{X}$, $\mathbf{C_X}$, is

$$\mathbf{C_X} = \mathbf{X}^\mathrm{T}\mathbf{X}. \tag{10}$$

Each eigenvector of $\mathbf{C_X}$, according to Pais et al. (2015), is an empirical orthogonal function (EOF) of $\mathbf{X}$, and represents a given spatial function. These are organised into an orthogonal matrix, $\mathbf{P}$, consisting of columns of EOFs, $\mathbf{p}_i$. We can then project $\mathbf{X}$ onto $\mathbf{P}$ to obtain

$$\mathbf{Y} = \mathbf{X}\mathbf{P}, \tag{11}$$

where the columns of $\mathbf{Y}$, $\mathbf{y}_i$, contain the principal components (PCs) of $\mathbf{X}$ (e.g. Pais et al., 2015). We can thus reconstruct $\mathbf{X}$ from N_p PCs and EOFs as

$$\hat{\mathbf{X}} = \mathbf{Y}\mathbf{P}^\mathrm{T} = \sum_{i=1}^{N_p} \mathbf{y}_i \mathbf{p}_i^\mathrm{T}. \tag{12}$$

Hence, the reconstructed flow coefficients are obtained from a linear combination of principal components of $\mathbf{X}$ and their associated eigenvectors for N_p modes, where $N_p \leq N_u$. In this paper, we reconstruct the flow associated with each individual pair of PC and EOF. We will interchangeably use the term PC to describe the temporal variation of the flow associated with that PC, and the reconstructed flow from that EOF-pair. This will be clear from the context. Finally, we obtain the associated eigenvalues for $\mathbf{p}_i$ from the covariance matrix of $\mathbf{Y}$. This is expressed as

$$\mathbf{C_Y} = \mathbf{P}^\mathrm{T}\mathbf{C_X}\mathbf{P} = \mathbf{\Lambda}, \tag{13}$$

where $\mathbf{\Lambda}$ is a diagonal matrix containing the eigenvalues, λ_i, associated with $\mathbf{p}_i$, ordered from largest to smallest.

3 Results

We invert 83 epochs of data from 1997.67 to 2025 with equation (8), using the conjugate gradient algorithm with Jacobi preconditioning, individually for each of our three flow models. We truncate the magnetic field at spherical harmonic degree $L_B = 14$ and the flow at spherical harmonic degree $L_u = 20$ for all three flows. The values of the damping parameters, λ_v and λ_t (and their sub-divisions for the TO-like and SA flows), the normalised rms misfit to the data, and the spatial norm (the value of the integral in equation (7) for all epochs), for all three models are given in Supplementary Table S2.1, and an analysis of the models' abilities to fit the data and their power spectra are given in Supplementary Section S1.

3.1 Investigating the flows

Figure 2 shows snapshots of the flow in 2007 and 2020. All three model types show the familiar features in core-flow, namely the westward-directed eccentric planetary gyre, with its enhanced high-latitude jet underneath the Bering Strait (the behaviour of the high-latitude jet is shown in Supplementary Figure S2.2). We also see, in 2007, very weak flow beneath the Pacific, which has turned into strong eastward flow by 2020. The flow is superimposed on the poloidal flow scalar, $\mathcal{S}$, which can serve as an indicator of up- ($\mathcal{S} > 0$) and down- ($\mathcal{S} < 0$) welling. The figures show, for all three flow types, the onset of an up-downwelling pair beneath the central and east equatorial Pacific, respectively, in 2020. This is in contrast to 2007, where there was very weak downwelling underneath the central equatorial Pacific, and some downwelling underneath South America. The growth of these up- and downwelling pairs were hypothesised by Grüne et al. (2025) to be related to the change in flow direction underneath the Pacific. The structure of the TO-like and minimum acceleration flows are very similar, as expected from their having the same spatial damping, whereas the SA flow is much stronger, and forcibly more equatorially symmetric.

Before decomposing the flows into their principal components, we investigate the temporal variation of the spatial statistics of the flow. These are shown in Figure 3. The minimum acceleration and TO-like flows are both ~85% toroidal, ~80% equatorially symmetric, and ~80% tangentially geostrophic (Le Mouël, 1984). This is comparable with other studies (e.g. Hulot et al., 1990; Amit and Olson, 2004; Beggan and Whaler, 2008; Amit and Pais, 2013; Grüne et al., 2025; Madsen et al., 2025). For the SA flows, the maximum amount of equatorial asymmetry we were able to force without noticeably decreasing the data-fit was ~8%, making it ~90% toroidal, ~92% equatorially symmetric, and ~85% tangentially geostrophic. These values vary over the model time-span, where all three models are slightly more equatorially symmetric from 2000 to 2010, slightly less equatorially symmetric from 2010 to 2020, and the equatorial symmetry increases again after 2020. The proportional energy of the toroidal flow that is focused in the zonal coefficients decreases from 1997 to 2020 for all three models, with the largest variation across the models shown by the TO-like flows, as expected.

3.2 Flow decomposition into principal components

Having investigated the behaviour of the three models, we now decompose each of them into their PCs. We undertake the decomposition in spectral space, jointly for the

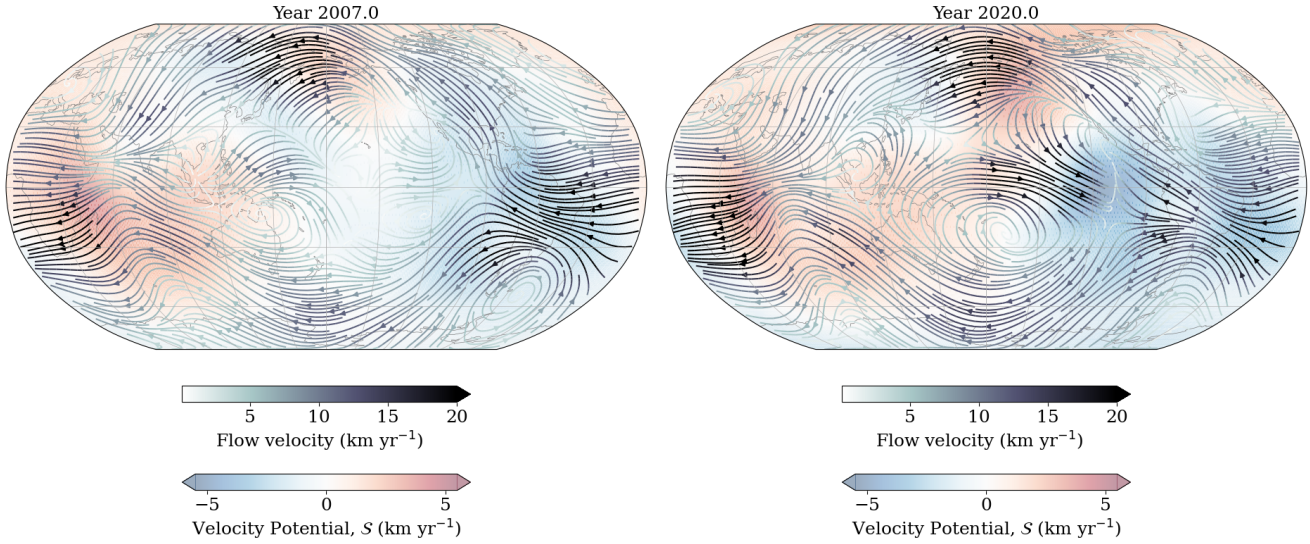

(a) Minimum acceleration

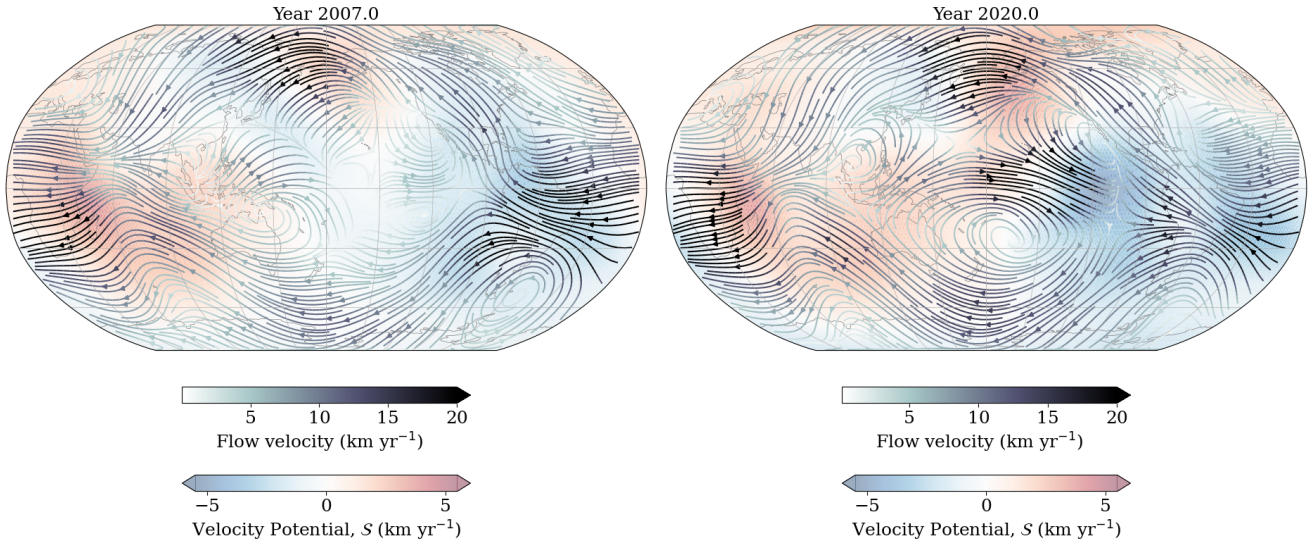

(b) TO-like

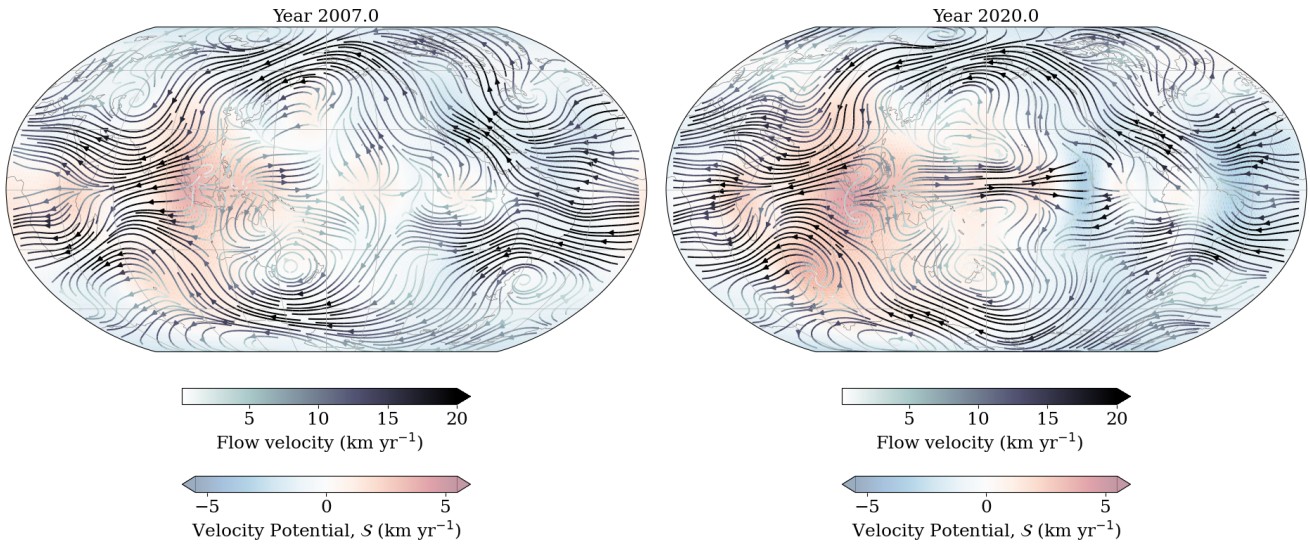

(c) SA

Figure 2: Snapshots of inverted core-surface flow for each of the three types of model. Flow is superimposed on poloidal flow potential, $\mathcal{S}$, where $\mathcal{S} > 0$ is indicative of fluid upwelling, and $\mathcal{S} < 0$ is indicative of downwelling. Plots are in Robinson projection, centred on 180° longitude, and continents are shown for reference only.

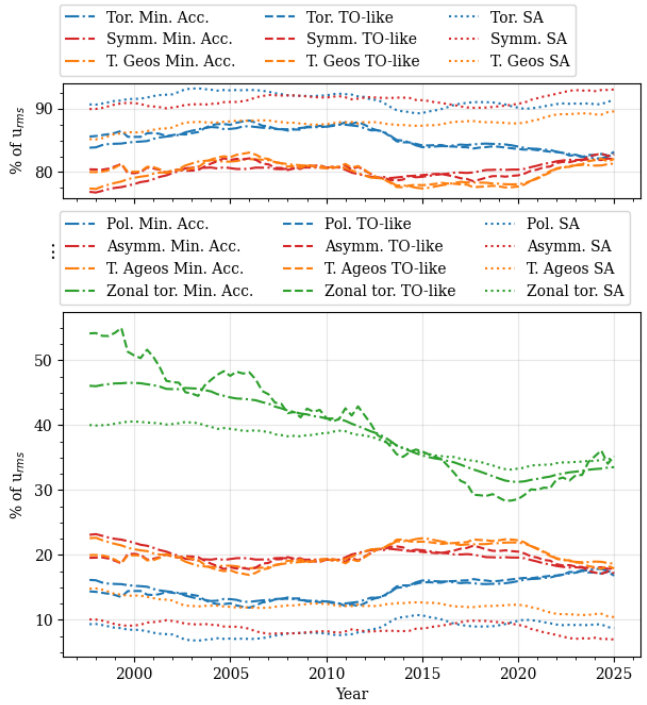

Figure 3: Temporal variation of the percentage spatial statistics of the minimum acceleration (dash-dotted line), TO-like (dotted line), and SA flow (dashed line). Note that top and bottom panel show different ranges of the same quantity. Abbreviations: Min. Acc. – Minimum acceleration; Symm. – Equatorially symmetric; T. Geos – Tangentially geostrophic; Asymm. – Equatorially antisymmetric; T. Ageos – Tangentially ageostrophic; Zonal tor. – Zonal toroidal.

toroidal and poloidal parts of the flow potential. All EOFs pass the degeneracy-check as defined by Pais et al. (2015) up to at least PC and EOF 13 for all models, and show energy above the "noise plateau" as discussed by Domingos et al. (2019) up to at least PC and EOF 20 (see Supplementary Figure S2.3). The first six PCs are shown in Figure 4. For all three flow types, > 99% of the total flow variance can be explained by the first two PCs. Toroidal PC 1 varies around $-10\,\mathrm{km\,yr^{-1}}$ for the minimum acceleration and TO-like flows and around $-12\,\mathrm{km\,yr^{-1}}$ for the SA flow, whereas poloidal PC 1 varies around $-1\,\mathrm{km\,yr^{-1}}$ for all flows. All three models have the same behaviour for PC 2, with both toroidal and poloidal PCs increasing from $\sim -2\,\mathrm{km\,yr^{-1}}$ in 1997.67, changing sign on either side of 2010 for poloidal and toroidal coefficients. The poloidal flow component continues to increase to $\sim 1.0\,\mathrm{km\,yr^{-1}}$ in 2015 and remains constant thereafter, whereas the toroidal flow component increases further to $\sim 2\,\mathrm{km\,yr^{-1}}$ in 2020, after which it decreases slightly. For the other PCs shown in Figure 4, there is broad agreement between all three models in PCs 1 to 6, and they show qualitatively similar phenomena, once the flow is evaluated on the core surface (as shown in Figure 5, S2.4 and S2.5). For this reason, we focus on the results from the minimum acceleration model from this point onwards. Results for the TO-like and SA models are given in the supplementary material.

Domingos et al. (2019) found, through analysing CHAMP and Swarm GVO data, that given the short temporal window of their study, their PCs could be approximated by Legendre polynomials of increasing degree, based on arguments by Gibson et al. (1992). We superimpose Legendre polynomials, $P_n(t)$ of increased degree, n, on our PCs in Figure 4, scaled to fit the PC for toroidal and poloidal flows separately. We see that there is good general agreement between PC n and $P_{n-1}(t)$, with the exception of PCs 4 and 5, that are best fit with $P_4(t)$ and $P_3(t)$, respectively. Gibson et al. (1992) indicate the approximation should be good in the so-called small-window regime, for which:

$$\epsilon = \left(\frac{2\sqrt{3\lambda_0}}{\sqrt{\lambda_1} N_t} \right)^2 \ll 1, \tag{14}$$

where λ_0 and λ_1 are the first two eigenvalues. We obtain a value of $\epsilon \sim eq 0.04$, which asserts us firmly within this regime.

In our analysis, we make the assumption that each PC of the toroidal flow can be combined with the same numbered PC of the poloidal flow, i.e., that each PC describes the same phenomenon, separately in the poloidal and toroidal coefficients. This is not necessarily the case. For example, Saraswati et al. (2023) analyse magnetic and gravitational core signals through similar means, and find that PC 1 of the magnetic secular acceleration corresponds to PC 2 of their joint magnetic and gravitational analysis. Therefore, to confirm if this assumption is valid (i.e. matching PCs like for like), we repeat the analysis, but by completing the PCA with the flow coefficients separately – in other words, by using only the toroidal or poloidal coefficients in $\mathbf{X}$ in equation (9). The results of this PCA are given in Supplementary Figures S2.6–S2.9. Comfortingly, we find that undertaking the PCA separately on the toroidal and poloidal flow coefficients produces a very similar result to computing their principal components together. The benefit to doing a separate PCA is that it allows the explained variance for toroidal and poloidal flows to be separated, which is not possible for the joint PCA. The joint PCA suggests that the first 2 PCs explain 99% of the flow variance, whereas the separate PCA suggests this is only true for the toroidal part of the flow (Supplementary Figure S2.6). However, as both components of the flow are deduced jointly by inversion, and the toroidal and poloidal flows are dynamically coupled, we concentrate henceforth on the results of joint PCA of the two sets of flow coefficients.

Figure 5 presents the first six PCs of the minimum acceleration model, as well as the associated flow evaluated on the core surface at two snapshots (individually selected for each PC), by combining the associated PC-EOF pairs through equation (12). PC 1 is associated with the eccentric gyre, with elevated flow strengths underneath the Bering strait, indicating the high-latitude jet (e.g. Livermore et al., 2017). The flow from PC 2 is concentrated in the region beneath the Pacific, with weak westward flow and negative $\mathcal{S}$ in the central equatorial Pacific in 2002, with regions of positive $\mathcal{S}$ on either side, i.e. beneath the Indian ocean and west equatorial Pacific. This changes to strong eastward flow and positive $\mathcal{S}$ in the central equatorial Pacific (with the snapshot shown for 2020), and negative $\mathcal{S}$ beneath the Indian ocean and west equatorial Pacific. The changeover happens in 2010 and has little associated flow outside of the central equatorial Pacific. PCs 3–5 appear to represent the up- and downwelling pairs underneath either side of the equatorial Pacific, as noted by Grüne et al. (2025). PCs 4–5 in particular are showing a quasi-decadal oscillation, which is reminiscent of the ~12 year oscillation identified by Gillet et al. (2024), also through PCA.

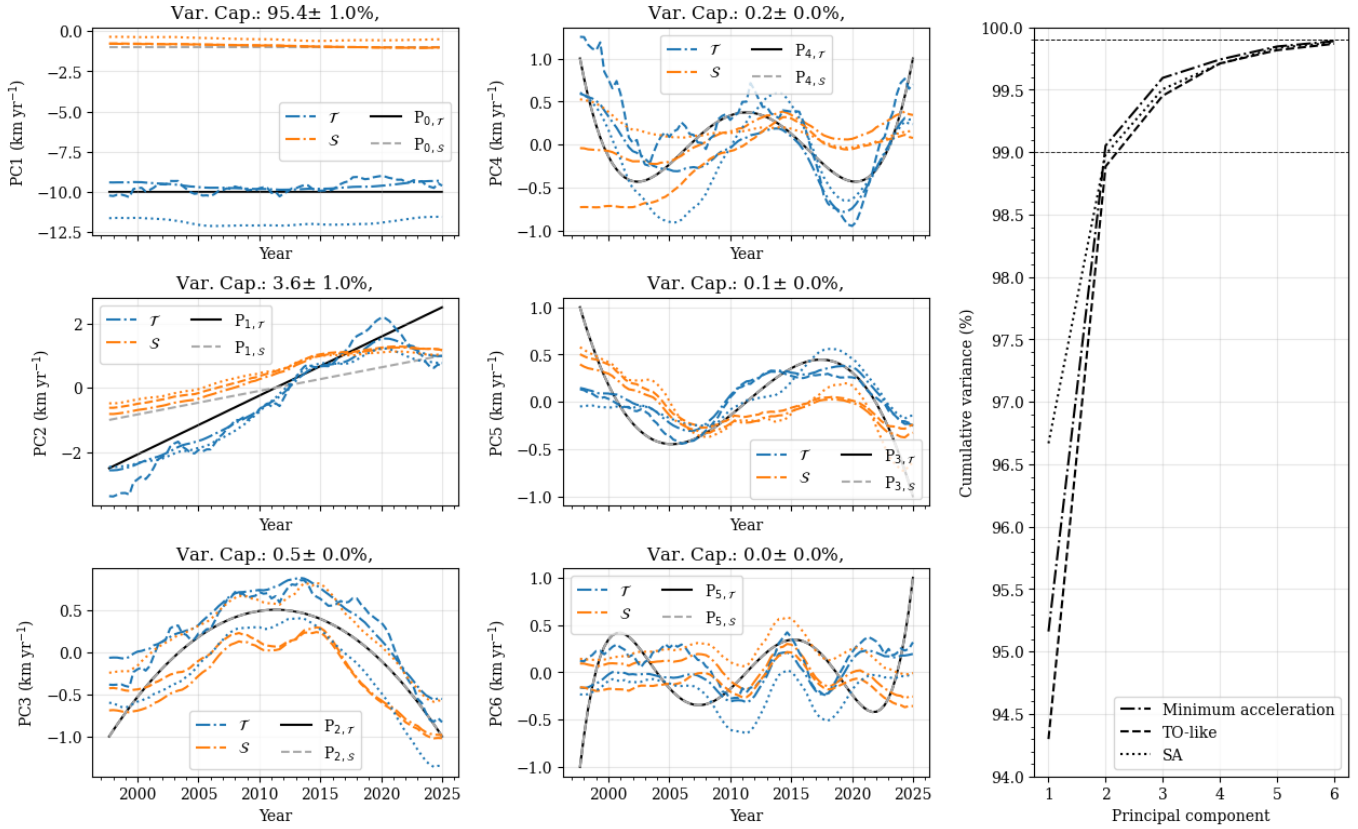

Figure 4: Temporal variability of principal components (PCs) 1–6, and their cumulative variance, for all three flows, where the minimum acceleration (dash-dotted line), TO-like (dotted line), and SA (dashed line) flows are similarly labelled to Figure 3. Normalised Legendre polynomials of matching degree, P_n, are shown in solid black for toroidal flow coefficients, and dashed gray for poloidal flow coefficients. Dashed lines indicate 99% and 99.9% variance. Abbreviations: Var. Cap. – Variance captured.

We note that the up-downwelling patterns shown by PC 4 are smaller scale than those shown by PC 5, i.e., these two PCs are not ranked by spatial length-scales. This is reminiscent of their fit to the Legendre polynomials in Figure 4, although those were fits to their temporal variability. Unexpectedly, PC 4 shows a strong upwelling towards the south pole, centred at 60°S. This corresponds to a region of the CMB within a magnetic field reverse flux patch (e.g. Kloss et al., 2026, Figure 10a), which is consequently a region where the poloidal flow is well resolved, and the toroidal flow is poorly resolved (Madsen et al., 2025). PC 6 represents flow that is centred beneath the central equatorial Pacific and the Indian ocean, with periodic variation of around a ~6 yr period after 2008, possibly highlighting the waves identified by Gillet et al. (2022). PCs 7–9 are shown in Supplementary Figure S2.10. PCs 7 and 8 do not appear to represent any easily identifiable physical phenomena, but PC 9 has similar periodic behaviour to PC 6, but from 2003–2011, and beneath the Atlantic rather than the Pacific. We attribute this to the Atlantic jerks occurring then, investigated by e.g. Chulliat and Maus (2014). It is possible that the periodic behaviour is related, carried westward by surface propagating core waves (e.g. Gillet et al., 2022; Grüne et al., 2025), although the wave velocity is too high to account for this. PCs beyond 9 carry less than 0.2% of the overall variance of the flow.

Predictions of the advected SV associated with PCs 1–2 and 3–9, and their sum, from equation (6), but reconfiguring $\mathbf{A}$ to only yield SV observations at Swarm altitude at the same three GVOs chosen in Figure S1.1, are shown in Figure 6, together with their CHAOS-8.3 (Kloss et al., 2026) values. Firstly, we note good agreement between the model predictions for the different combinations of PCs, despite the differences in behaviour of some of the PCs individually. Figure 6 confirms that PCs 1–2 are mostly responsible for the large-scale SV change, whereas PCs 3–9 recreate the shorter timescale variations, such as geomagnetic jerks. As expected, since the first 9 PCs correspond to 99.8% of the overall flow variance, the advected SV associated with these PCs is able to recreate most of the SV modelled by CHAOS.

3.3 Isolating the planetary gyre and the Pacific overturn

We now focus on the first two principal components, in order to isolate the planetary gyre (PC 1) and the Pacific flow overturn (PC 2). These PCs have spatial power concentrated in spherical harmonic degrees 1-4 (PC 1) and 2-6 (PC 2), shown explicitly in Supplementary Figure S2.11. Figure 7 presents the combined eigenvectors of PCs 1–2, snapshots of the flow in 2007 and 2020, and their advected radial SV at Swarm altitude from 1997.67–2025 at 300 GVOs. The upper panel of Figure 7 shows that the advected SV associated with these PCs is responsible for increased secular acceleration beneath the Pacific, particularly around 150°E and 150°W, with a band of weak secular acceleration between them around 180°. This spatial distribution of constant secular acceleration is associated with PC 2, whereas the slower changes in SV observed outside of the Pacific are associated with the planetary gyre. The figure also shows that in 2020, at the time where the

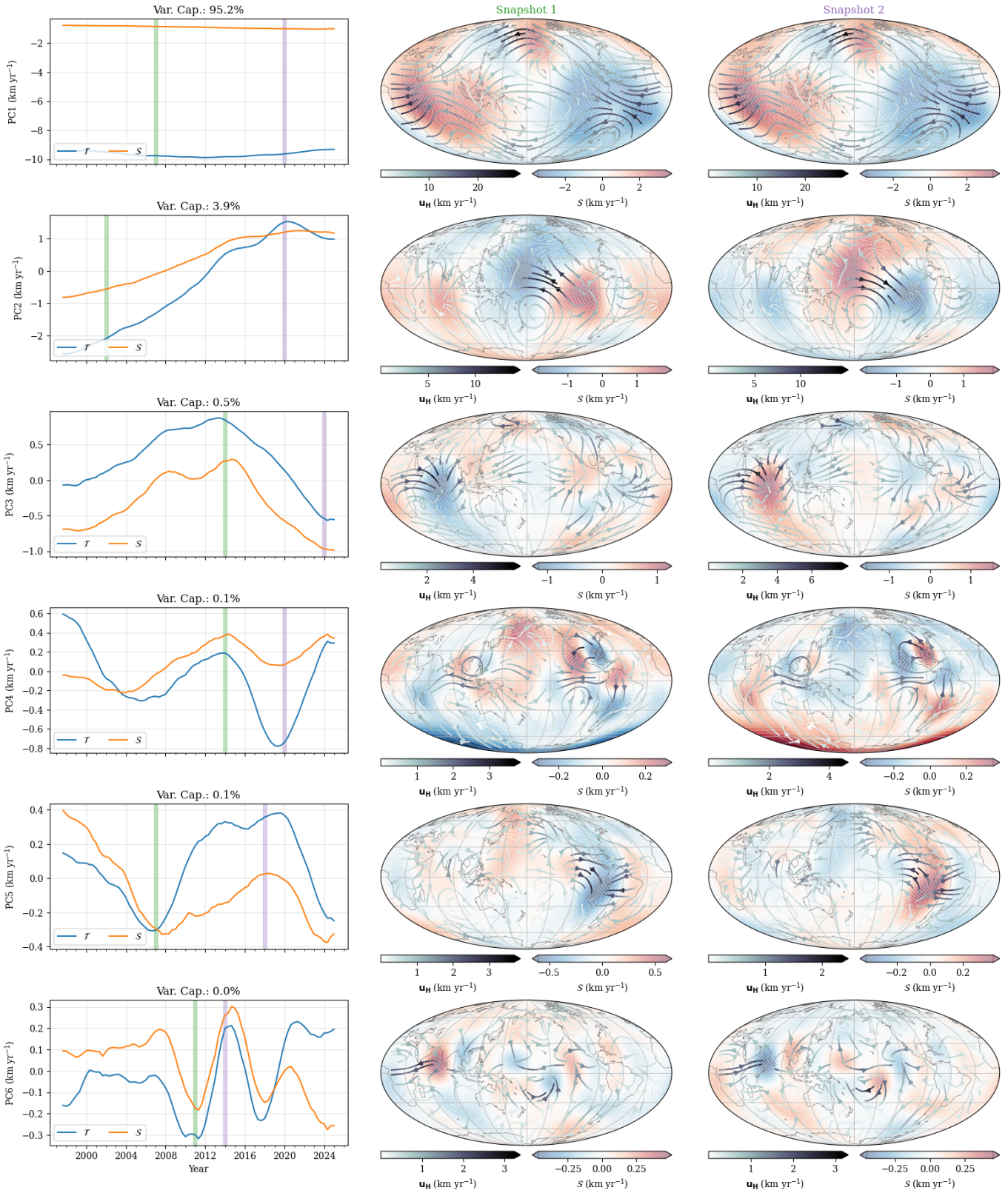

Figure 5: (Left) Temporal changes of the first 6 principal components (PCs) of the toroidal and poloidal flow from the minimum acceleration model, with the times of the flow snapshots to the right marked in green (first snapshot) and purple (second snapshot). (Right) Snapshots of the flows associated with the PCs. Flow is superimposed on poloidal flow potential, $\mathcal{S}$, where $\mathcal{S} > 0$ is indicative of fluid upwelling, and $\mathcal{S} < 0$ is indicative of downwelling. Note that the colour scales change for each principal component. Rows represent individual PCs (PC1 = first row, PC2 = second row, and so on). Plots are in Mollweide projection, centred on 180° longitude, and continents are shown for reference only. Note that flow and flow potential colour scales change with each plot. Abbreviations: Var. Cap. – Variance captured.

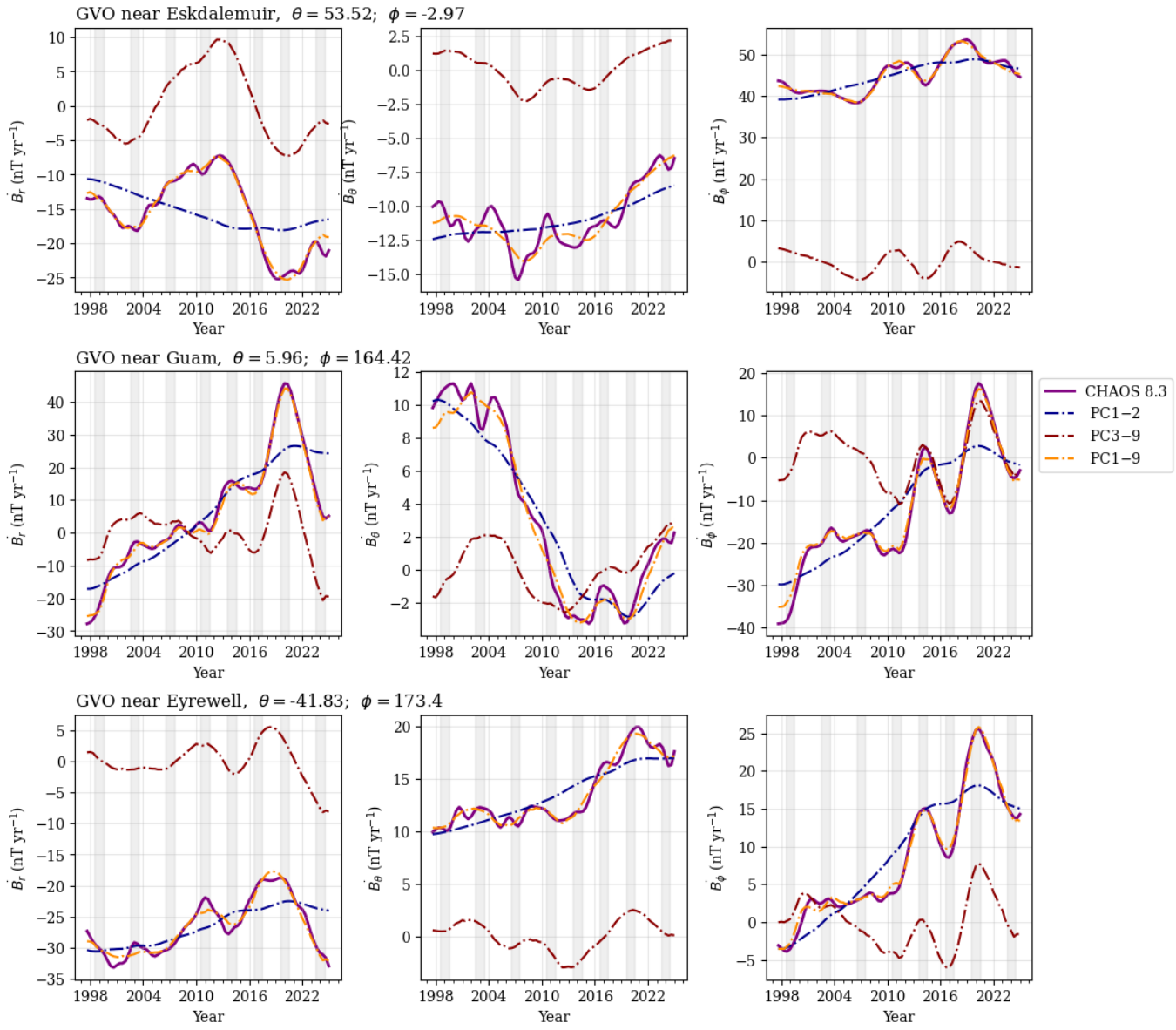

Figure 6: Advected SV at Swarm altitude ($r = 6861.20$ km) at three GVOs, from PC 1–2 (blue), PC 3–9 (red), and their sum (PC 1–9, orange), for the minimum acceleration model, and compared to CHAOS-8.3 (Kloss et al., 2026) (purple). Timings of geomagnetic jerks (1999: Mandea et al. (2000); 2003: Wardinski et al. (2008); 2007: Chulliat et al. (2010); 2011: Chulliat and Maus (2014); 2014: Torta et al. (2015); 2017: Whaler et al. (2022); 2020: Pavón-Carrasco et al. (2021); 2024: Madsen et al. (2025)) are shaded in grey.

principal component peaks, there is an inflection in the SV record around the Pacific, associated with the 2020 geomagnetic jerk (e.g. Pavón-Carrasco et al., 2021; Madsen et al., 2025). As jerks are associated with changes in secular acceleration (e.g. Brown et al., 2013; Pinheiro et al., 2019), this suggests that the increase in flow-amplitude stopped in 2020, and it may be decreasing again.

4 Discussion

In this paper, we have investigated the principal components of core-surface flow over the past 27 years. Our PCA decomposed the flow into three major components: a stable gyre with a high-latitude jet (PC 1), an overturning west-to-east flow in the equatorial Pacific (PC 2), and isolated up- and downwelling pairs and wave-like patterns in the equatorial region (PCs 3-9). Similar results were reported by Li et al. (2024), who analysed a neural network-derived flow using dynamic mode decomposition, and by Ropp and Lesur (2023), who performed PCA on their co-estimated flow and magnetic field model, constrained by statistics from geodynamo simulations. As mentioned in Section 2.3, PCA has already been used to isolate spatial features of wave patterns. Gillet et al. (2024) found waves of periods of 3.5, 6.5, and 12.5 years focused along the equatorial region, particularly underneath the Atlantic and Pacific, since at least 1958. This suggests that they are indeed long-term features of core-flow, and despite being associated with $< 1\%$ of the core-surface flow variance, they are responsible for much of the intradecadal and decadal variation in SV, as we show in Figure 6.

Through PCA, we have shown that the eccentric planetary gyre accounts for the majority of the flow variance over the past 27 years. In particular, it accounts for $96.6 \pm 0.8\%$ of the toroidal flow variance, and $82.0 \pm 1.4\%$ of the poloidal flow variance (evaluated with separate PCA for toroidal and poloidal flow coefficients, see Figure S2.6), comparing our three different types of models with different spatial and temporal constraints. All three flow types indicate very little change in the flow associated with the gyre over the timespan of the model, with the only change being an increase in poloidal flow underneath the high latitude jet. This is in agreement with the results from other studies (e.g. Gillet et al., 2022; Ropp and Lesur, 2023; Finlay et al., 2023).

So how does the presence of a stable gyre relate to the overturn of flow in the Pacific? Given that the stable gyre dominates the Atlantic hemisphere at low- to mid-latitudes, this leaves low latitude flow in the Pacific hemisphere unaffected. Therefore, a separate flow regime – independent of the gyre – could exist in this region. Incidentally, 2010 marks the onset of disruption to the dominant 6 year oscillations in ΔLOD, returning in amplitude (but changed in phase) in 2014, as was reported by Madsen and Holme (2025). Similar conclusions were drawn by Saraswati et al. (2023) and Sidorov et al. (2025), who investigated period changes in the magnetic field. The alteration to the flow beneath the Pacific, and the interruption in the 6-year oscillation, are also contemporary with change in inner-core seismic signature (Yang and Song, 2023; Wang et al., 2024; Vidale et al., 2025; Wu et al., 2026). It also marks the rise of magnetic waves propagating along the core surface in the Pacific region after 2014 (e.g Gillet et al., 2022; Ropp and Lesur, 2023; Gillet et al., 2024; Grüne et al., 2025). It could therefore be that the overturn of the flow beneath the Pacific is linked to the rise of fast waves there after the 2010s (e.g Gillet et al., 2024; Madsen et al., 2025; Grüne et al., 2025), which could both be triggered by a singular event happening deeper in the core. An alternative explanation for the sudden rise of eastward flow is heterogeneous CMB heat flow. Mound and Davies (2023) found through numerical dynamo simulations that regions of increased heat flow gives rise to eastward flow, suggesting that this feature may be driven by the thermal wind, i.e. from above, rather than by the deeper core. This offers an explanation for a preferential flow direction underneath the Pacific, given that the heterogeneous heat flow structure at the CMB is a long-lived feature.

Here, we utilised the three modelling approaches of Madsen et al. (2025) to investigate whether temporal or spatial restrictions on the flow have an impact on the resolved overturn of the Pacific flow, especially when compared to a spatiotemporally unconstrained flow. As was discussed by Madsen et al. (2025), this is inspired by the ill-determined nature of core-flow modelling, where obtaining a unique flow from the induction equation requires further assumptions. Some physical assumptions frequently imposed are tangential geostrophy (Le Mouël, 1984), columnar flow (Amit and Olson, 2004), or quasi-geostrophy (Pais and Jault, 2008; Gillet et al., 2009), or fitting the energy spectrum of the flow to geodynamo simulations (e.g. Ropp and Lesur, 2023; Istas et al., 2023; Aubert, 2023; Rogers et al., 2025). In the example of quasi-geostrophic flows and columnar flows, equatorial symmetry is implied, and is often enforced when using the tangentially geostrophic assumption (e.g. Gillet et al., 2009; Amit and Pais, 2013). Our results suggest that all our three flow model types qualitatively fit the observations equally well, in that they all have very similar normalised rms misfits to the data, as was similarly found by Madsen et al. (2025) when modelling CHAMP- or Swarm-only data. However, their data-series were conveniently separated into before the Pacific overturn (CHAMP, 2001–2010) and after (Swarm, 2014–2023). The models in this paper cover the whole time period, and Figure S1.1 shows that the SV data predictions by SA flows at ground observatories in the west Pacific (Guam and Eyrewell) are slightly but systematically offset from the other model predictions, and the data, after 2010. This is most clear in the $\dot{B}_\phi$ component from Guam (Figure S1.1c) and $\dot{B}_r$ and $\dot{B}_\theta$ from Eyrewell (Figure S1.1e). Any differences are less clear in the GVO data, possibly because of their increased altitude. It is therefore likely that, although the SA models are able to explain the cross-equatorial flow underneath Indonesia (e.g. Figure 2, and Madsen et al., 2025), more equatorial anti-symmetry than its ~10% (Figure 3) is required to account completely for the overturning of flow beneath the Pacific.

5 Conclusion

We inverted ground and satellite observatory SV data for time-dependent core-surface flow models over 27 years, using three different modelling techniques. With the SA flows, we found that the minimum required amount of equatorial asymmetry in the flow to explain the data is around 10%, whereas our TO-like and minimum acceleration flows, which are geometrically unconstrained, are ~80% toroidal, equatorially symmetric, and tangentially geostrophic, and that this

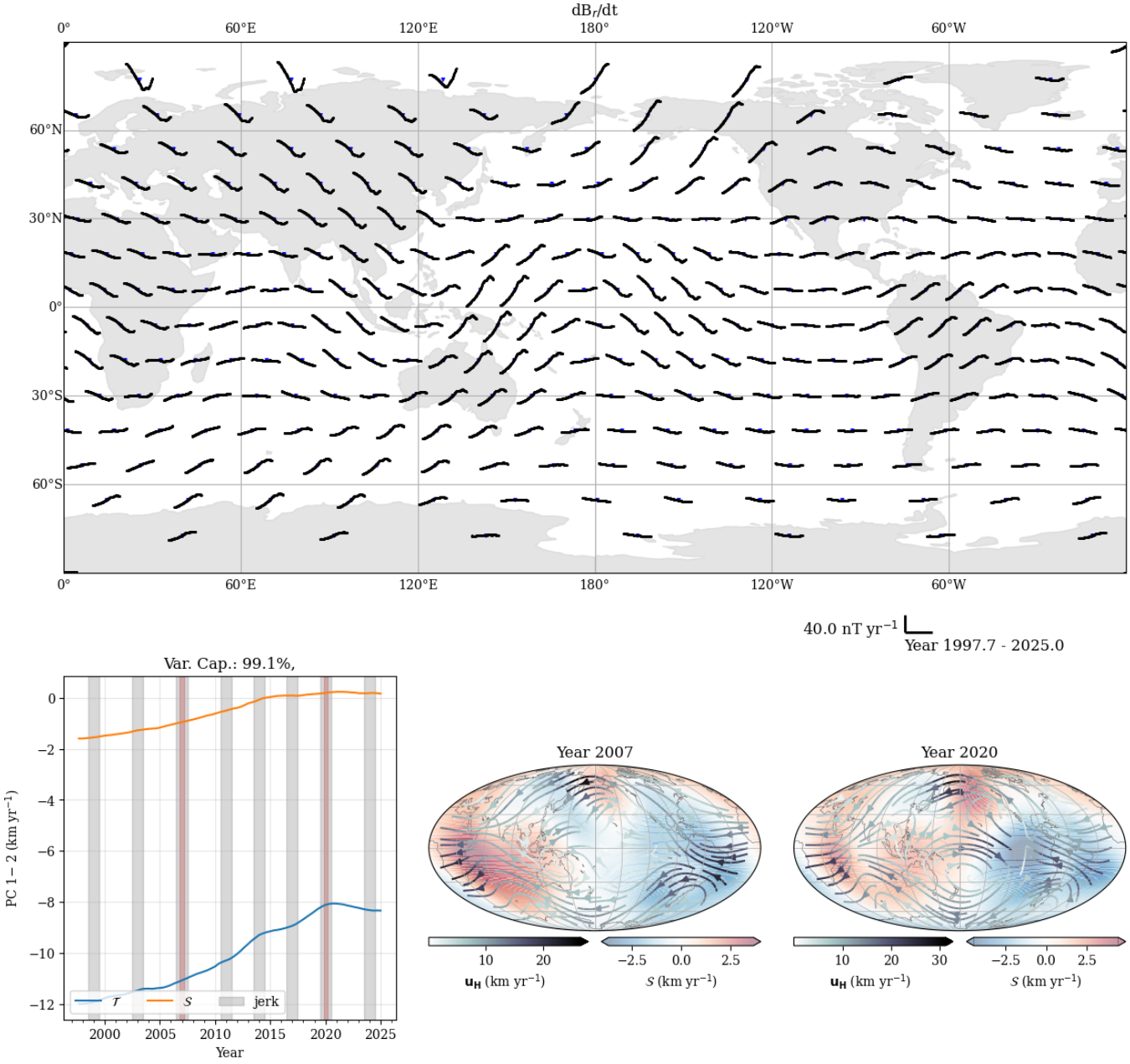

Figure 7: Sum of principal components 1–2 of the minimum acceleration model. Upper panel: the advected radial SV generated from this part of the flow at Swarm altitude ($r = 6861.20$ km) at 300 GVOs; lower panel: the sum of the first two eigenvectors of the flow, with timings of geomagnetic jerks superimposed (1999: Mandea et al. (2000); 2003: Wardinski et al. (2008); 2007: Chulliat et al. (2010); 2011: Chulliat and Maus (2014); 2014: Torta et al. (2015); 2017: Whaler et al. (2022); 2020: Pavón-Carrasco et al. (2021); 2024: Madsen et al. (2025)), and snapshots of this part of the flow in 2007 and 2020 (highlighted on the time axis in red). Flow is superimposed on poloidal flow potential, $\mathcal{S}$, where $\mathcal{S} > 0$ is indicative of fluid upwelling, and $\mathcal{S} < 0$ is indicative of downwelling, plotted in Mollweide projection, centred on 180° longitude, with continents shown for reference only. Abbreviations: Var. Cap. – Variance captured.

spatial distribution remains fairly constant throughout the model period. All three of our models show that the flow underneath the Pacific reversed from being weakly westward prior to 2010, to being an accelerating strong eastward flow after 2010. By decomposing the flow into its principal components, we find that ~90% of the flow variance is described by the first principal component, an almost steady eccentric planetary gyre and high-latitude jet. We then isolate overturning flow beneath the Pacific in the second principal component, which explains another ~10% of the flow variance. This principal component suggests that the Pacific eastward flow has been weakening again since 2020. The remaining PCs account for ~1% of the flow variance and include standing and propagating waves at the core surface, and also generate geomagnetic jerk signals in the SV by advection, as shown in Figure 6. Finally, we hypothesise that the overturn of flow underneath the Pacific is a consequence of events triggered in the deeper core in 2010, as observed from seismological and geodetic studies, although we note that eastward flow could be a consequence of heterogeneous heat flow across the CMB.

Acknowledgements

The results presented here include data collected at magnetic observatories. We thank the national institutes that support them and INTERMAGNET for promoting high standards of magnetic observatory practice (https://intermagnet.org). We thank DTU for processing the satellite data and preprocessing the ground observatory data for our purposes. FDM and IH were supported by a NERC Doctoral Training Partnership grant (NE/S007407/1), and FDM was in part funded by BGS University Funding Initiative PhD studentship S493. WB was supported by the British Geological Survey via NERC national capability. KAW was supported partly by ESA through the Swarm DISC activities, funded by ESA contract no. 4000109587. Comments from Mathieu Dumberry and Nicolas Gillet significantly improved the manuscript.

Data Availability

- The Swarm GVOs are available through the Swarm DISC server: https://swarm-diss.eo.esa.int/#swarm%2FLevel2longterm%2FVOB
- The Ørsted, CHAMP, and CryoSat-2 GVOs are available from Danish Technical University through the following link: https://www.space.dtu.dk/english/research-divisions/geomagnetism-and-geospace/projects/geomagnetic-virtual-observatories
- The GO data was processed by the Danish Technical University, and is available upon request. The hourly means data are available through the British Geological Survey: https://auxobs-api.bgs.ac.uk/docs
- CHAOS-8 coefficients are available through https://www.spacecenter.dk/files/magnetic-models/CHAOS-8/

Competing interests

We confirm that the authors have no competing interests.

Abbreviations

- SV = Secular variation
- Var. Cap. = Variance captured
- CMB = Core mantle boundary
- PCA = Principal component analysis
- PC = Principal component
- EOF = Empirical orthogonal function
- SA = symmetric-asymmetric
- TO = Torsional oscillation
- LOD = Length-of-day
- GVO = Geomagnetic virtual observatory
- rms = Root-mean-square

References

Amit, H. and P. Olson (2004). Helical core flow from geomagnetic secular variation. *Phys. Earth Planet. Inter.* 147.1, 1–25. DOI: 10.1016/J.PEPI.2004.02.006.

Amit, H. and M. A. Pais (2013). Differences between tangential geostrophy and columnar flow. *Geophys. J. Int.* 194.1, 145–157. DOI: 10.1093/gji/ggt077.

Aubert, J. (2023). State and evolution of the geodynamo from numerical models reaching the physical conditions of Earth's core. *Geophys. J. Int.* 235.1, 468–487. DOI: 10.1093/gji/ggad229.

Beggan, C. and K. Whaler (2008). Core flow modelling assumptions. *Phys. Earth Planet. Inter.* 167.3-4, 217–222. DOI: 10.1016/J.PEPI.2008.04.011.

Bloxham, J. (1988). The determination of fluid flow at the core surface from geomagnetic observations. *Mathematical Geophysics: A Survey of Recent Developments in Seismology and Geodynamics*. Ed. by N. J. Vlaar, G. Nolet, M. J. R. Wortel, and S. A. P. L. Cloetingh. Dordrecht: Springer Netherlands, pp. 189–208. DOI: 10.1007/978-94-009-2857-2_9.

Brown, W. J., J. E. Mound, and P. W. Livermore (2013). Jerks abound: An analysis of geomagnetic observatory data from 1957 to 2008. *Phys. Earth Planet. Inter.* 223, 62–76. DOI: 10.1016/J.PEPI.2013.06.001.

Cain, J. C., Z. Wang, D. R. Schmitz, and J. Meyer (1989). The geomagnetic spectrum for 1980 and core-crustal separation. *Geophys. J. Int.* 97.3, 443–447. DOI: 10.1111/j.1365-246X.1989.tb00514.x.

Chulliat, A. and S. Maus (2014). Geomagnetic secular acceleration, jerks, and a localized standing wave at the core surface from 2000 to 2010. *J. Geophys. Res.: Solid Earth* 119.3, 1531–1543. DOI: 10.1002/2013JB010604.

Chulliat, A., E. Thébault, and G. Hulot (2010). Core field acceleration pulse as a common cause of the 2003 and 2007 geomagnetic jerks. *Geophys. Res. Lett.* 37.7. DOI: 10.1029/2009GL042019.

Claveau, R., N. Gillet, P.-O. Amblard, and C. C. Finlay (2025). Broadband a priori temporal cross-covariances for the geomagnetic inverse problem: application to the satellite era. *Earth, Planets and Space* 77.1, 126. DOI: 10.1186/s40623-025-02248-z.

Courtillot, V., J. Ducruix, and J. L. Le Mouël (1978). Sur une acceleration recente de la variation seculaire du champ magnetique terrestre. *C. R. Acad. Sci. D* 287.12, 1095–1098.

Domingos, J., M. A. Pais, D. Jault, and M. Mandea (2019). Temporal resolution of internal magnetic field modes from satellite data. *Earth, Planets and Space* 71.1, 2. DOI: 10.1186/s40623-018-0983-5.

Finlay, C. C., N. Gillet, J. Aubert, P. W. Livermore, and D. Jault (2023). Gyres, jets and waves in the Earth's core. *Nature Reviews Earth & Environment*. DOI: 10.1038/s43017-023-00425-w.

Friis-Christensen, E., H. Lühr, and G. Hulot (2006). Swarm: A constellation to study the Earth's magnetic field. *Earth, Planets and Space* 58.4, 351–358. DOI: 10.1186/BF03351933.

Gibson, J. F., J. Doyne Farmer, M. Casdagli, and S. Eubank (1992). An analytic approach to practical state space reconstruction. *Physica D: Nonlinear Phenomena* 57.1-2, 1–30. DOI: 10.1016/0167-2789(92)90085-2.

Gillet, N., F. Dall'Asta, P.-O. Amblard, R. Claveau, and J. Aubert (2024). Waves in Earth's core and geomagnetic field forecast. *Phys. Earth Planet. Inter.* 357, 107284. DOI: 10.1016/j.pepi.2024.107284.

Gillet, N., L. Huder, and J. Aubert (2019). A reduced stochastic model of core surface dynamics based on geodynamo simulations. *Geophys. J. Int.* 219.1, 522–539. DOI: 10.1093/gji/ggz313.

Gillet, N., M. A. Pais, and D. Jault (2009). Ensemble inversion of time-dependent core flow models. *Geochem. Geophys. Geosyst.* 10.6. DOI: 10.1029/2008GC002290.

Gillet, N., F. Gerick, D. Jault, T. Schwaiger, J. Aubert, and M. Istas (2022). Satellite magnetic data reveal interannual waves in Earth's core. *Proc. Nat. Acad. Sci. USA* 119.13, e2115258119. DOI: 10.1073/pnas.2115258119.

Grüne, C. R., K. A. Whaler, and F. D. Madsen (2025). Detecting low-latitude outer core-surface waves with 25 years of satellite secular variation data. *Phys. Earth Planet. Inter.*, 107435. DOI: 10.1016/J.PEPI.2025.107435.

Gubbins, D. and P. H. Roberts (1987). Magnetohydrodynamics of the Earth's core. *Geomagnetism*. Ed. by J. A. Jacobs. 1st. Vol. 2. Academic Press, pp. 1–183.

Hammer, M. D., G. A. Cox, W. J. Brown, C. D. Beggan, and C. C. Finlay (2021). Geomagnetic Virtual Observatories: monitoring geomagnetic secular variation with the Swarm satellites. *Earth, Planets and Space* 73, 54. DOI: 10.1186/s40623-021-01357-9.

Hammer, M. D., C. C. Finlay, and N. Olsen (2021). Applications for CryoSat-2 satellite magnetic data in studies of Earth's core field variations. *Earth, Planets and Space* 73.1, 73. DOI: 10.1186/s40623-021-01365-9.

Holme, R. (2015). 8.04 - Large-Scale Flow in the Core. *Treatise on Geophysics (Second Edition)*. Ed. by G. Schubert. Oxford: Elsevier, pp. 91–113. DOI: 10.1016/B978-0-444-53802-4.00138-X.

Howard, I., I. Buckroyd, A. Mohn, and F. D. Madsen (2025). Hilbert-Huang Transform Analysis of Intradecadal Variations in the Length of Earth's Day. *Edinburgh Student Journal of Science* 2, 1–5. DOI: 10.2218/esjs.11674.

Hulot, G., J.-L. Le Mouël, and D. Jault (1990). The flow at the core-mantle boundary: Symmetry properties. *J. Geomag. Geoelecr.* 42.7, 857–874. DOI: 10.5636/jgg.42.857.

Istas, M., N. Gillet, C. C. Finlay, M. D. Hammer, and L. Huder (2023). Transient core surface dynamics from ground and satellite geomagnetic data. *Geophys. J. Int.* 233.3, 1890–1915. DOI: 10.1093/gji/ggad039.

Jackson, A., A. R. T. Jonkers, and M. R. Walker (2000). Four centuries of geomagnetic secular variation from historical records. *Phil. Trans. R. Soc. Lond. A: Mathematical, Physical and Engineering Sciences* 358.1768, 957–990. DOI: 10.1098/rsta.2000.0569.

Jault, D., P. Personnettaz, N. Gillet, T. Lepage, and N. Schaeffer (2026). Viscous and Magnetic Boundary Layers at the Top of the Core in Geodynamo Models. *J. Geophys. Res.* (In revision).

Jolliffe, I. T. (2002). Principal component analysis. Second edition. Springer series in statistics. New York ; Springer-Verlag. DOI: 10.1007/b98835.

Kloss, C., C. C. Finlay, N. Olsen, L. Tøffner-Clausen, N. Gillet, and A. Grayver (2026). The CHAOS-8 geomagnetic field model. *Earth, Planets and Space* 78.1, 21. DOI: 10.1186/s40623-025-02352-0.

Le Mouël, J. L. (1984). Outer-core geostrophic flow and secular variation of Earth's geomagnetic field. *Nature* 311.5988, 734–735. DOI: 10.1038/311734A0.

Li, J., Y. Lin, and K. Zhang (2024). Dynamic Mode Decomposition of the Core Surface Flow Inverted From Geomagnetic Field Models. *Geophys. Res. Lett.* 51.1. DOI: 10.1029/2023GL106362.

Livermore, P. W., R. Hollerbach, and C. C. Finlay (2017). An accelerating high-latitude jet in Earth's core. *Nat. Geosci.* 10.1, 62–68. DOI: 10.1038/ngeo2859.

Macmillan, S. and N. Olsen (2013). Observatory data and the Swarm mission. *Earth, Planets and Space* 65.11, 1355–1362. DOI: 10.5047/eps.2013.07.011.

Madsen, F. D., C. D. Beggan, W. J. Brown, R. Holme, J. B. Lauridsen, and K. A. Whaler (2026). IGRF-14 secular variation prediction from core surface flow acceleration. *Earth, Planets and Space* 78.1, 29. DOI: 10.1186/s40623-025-02347-x.

Madsen, F. D. and R. Holme (2025). A recent interruption in the 6-year oscillation in length-of-day. *Geophys. J. Int.* 243.2, ggaf337. DOI: 10.1093/gji/ggaf337.

Madsen, F. D., K. A. Whaler, C. D. Beggan, W. J. Brown, J. B. Lauridsen, and R. Holme (2025). Modelling geomagnetic jerks with core surface flow derived from satellite gradient tensor elements of secular variation. *Phys. Earth Planet. Inter.* 366, 107336. DOI: 10.1016/j.pepi.2025.107336.

Mandea, M. and N. Olsen (2006). A new approach to directly determine the secular variation from magnetic satellite observations. *Geophys. Res. Lett.* 33.15. DOI: 10.1029/2006GL026616.

Mandea, M., E. Bellanger, and J. L. Le Mouël (2000). A geomagnetic jerk for the end of the 20th century? *Earth Planet. Sci. Lett.* 183.3-4, 369–373. DOI: 10.1016/S0012-821X(00)00284-3.

Mound, J. E. and C. J. Davies (2023). Longitudinal structure of Earth's magnetic field controlled by lower mantle heat flow. *Nat. Geosci.* DOI: 10.1038/s41561-023-01148-9.

Neubert, T., M. Mandea, G. Hulot, R. von Frese, F. Primdahl, J. L. Jørgensen, E. Friis-Christensen, P. Stauning, N. Olsen, and T. Risbo (2001). Ørsted satellite captures high-precision geomagnetic field data. *Eos, Transactions American Geophysical Union* 82.7, 81–88. DOI: 10.1029/01EO00043.

Olsen, N., H. Lühr, C. C. Finlay, T. J. Sabaka, I. Michaelis, J. Rauberg, and L. Tøffner-Clausen (2014). The CHAOS-4

geomagnetic field model. *Geophys. J. Int.* 197.2, 815–827. DOI: 10.1093/gji/ggu033.

Pais, M. A. and D. Jault (2008). Quasi-geostrophic flows responsible for the secular variation of the Earth's magnetic field. *Geophys. J. Int.* 173.2, 421–443. DOI: 10.1111/j.1365-246X.2008.03741.x.

Pais, M. A., A. L. Morozova, and N. Schaeffer (2015). Variability modes in core flows inverted from geomagnetic field models. *Geophys. J. Int.* 200.1, 402–420. DOI: 10.1093/gji/ggu403.

Pavón-Carrasco, F. J., S. Marsal, S. A. Campuzano, and J. M. Torta (2021). Signs of a new geomagnetic jerk between 2019 and 2020 from Swarm and observatory data. *Earth, Planets and Space* 73.1, 175. DOI: 10.1186/s40623-021-01504-2.

Pinheiro, K. J., H. Amit, and F. Terra-Nova (2019). Geomagnetic jerk features produced using synthetic core flow models. *Phys. Earth Planet. Inter.* 291, 35–53. DOI: 10.1016/j.pepi.2019.03.006.

Reigber, C. (2004). Earth Observation with CHAMP: Results from Three Years in Orbit. Ed. by C. Reigber, H. Lühr, Peter Schwintzer, and Jens Wickert. Potsdam: Springer. DOI: 10.1007/b138105.

Roberts, P. H. and S. Scott (1965). On Analysis of the Secular Variation — 1. A Hydromagnetic Constraint: Theory. *J. Geomag. Geoelecr.* 17.2, 137–151. DOI: 10.5636/jgg.17.137.

Rogers, H. F., N. Gillet, J. Aubert, P. Personnettaz, and M. Mandea (2025). Effects of geodynamo priors and geomagnetic data on inverted core surface flows. *Phys. Earth Planet. Inter.*, 107323. DOI: 10.1016/j.pepi.2025.107323.

Ropp, G. and V. Lesur (2023). Mid-latitude and equatorial core surface flow variations derived from observatory and satellite magnetic data. *Geophys. J. Int.* 234.2, 1191–1204. DOI: 10.1093/gji/ggad113.

Saraswati, A. T., O. de Viron, and M. Mandea (2023). Earth's core variability from magnetic and gravity field observations. *Solid Earth* 14.12, 1267–1287. DOI: 10.5194/se-14-1267-2023.

Sidorov, R., A. Soloviev, and S. Bogoutdinov (2025). A 6-year quasi-periodicity in the geomagnetic secular acceleration pulses over 1932–2022. *Phys. Earth Planet. Inter.* 361, 107330. DOI: 10.1016/j.pepi.2025.107330.

Suttie, N., A. Nilsson, N. Gillet, and M. Dumberry (2025). Large-scale palaeoflow at the top of Earth's core. *Earth Planet. Sci. Lett.* 652, 119185. DOI: 10.1016/J.EPSL.2024.119185.

Teed, R. J., C. A. Jones, and S. M. Tobias (2019). Torsional waves driven by convection and jets in Earth's liquid core. *Geophys. J. Int.* 216.1, 123–129. DOI: 10.1093/gji/ggy416.

Torta, J. M., F. J. Pavón-Carrasco, S. Marsal, and C. C. Finlay (2015). Evidence for a new geomagnetic jerk in 2014. *Geophys. Res. Lett.* 42.19, 7933–7940. DOI: 10.1002/2015GL065501.

Tsang, Y.-K. and C. A. Jones (2024). Scaling of the geomagnetic secular variation timescale. *Geophys. J. Int.* 239.1, 1–16. DOI: 10.1093/gji/ggae234.

Vidale, J. E., W. Wang, R. Wang, G. Pang, and K. Koper (2025). Annual-scale variability in both the rotation rate and near surface of Earth's inner core. *Nat. Geosci.* 18.3, 267–272. DOI: 10.1038/s41561-025-01642-2.

Wang, W., J. E. Vidale, G. Pang, K. D. Koper, and R. Wang (2024). Inner core backtracking by seismic waveform change reversals. *Nature* 631.8020, 340–343. DOI: 10.1038/s41586-024-07536-4.

Wardinski, I., R. Holme, S. Asari, and M. Mandea (2008). The 2003 geomagnetic jerk and its relation to the core surface flows. *Earth Planet. Sci. Lett.* 267.3-4, 468–481. DOI: 10.1016/J.EPSL.2007.12.008.

Whaler, K. A. (1986). Geomagnetic evidence for fluid upwelling at the core-mantle boundary. *Geophys. J. R. Astr. Soc.* 86.2, 563–588. DOI: 10.1111/j.1365-246X.1986.tb03844.x.

Whaler, K. A., M. D. Hammer, C. C. Finlay, and N. Olsen (2022). Core Surface Flow Changes Associated With the 2017 Pacific Geomagnetic Jerk. *Geophys. Res. Lett.* 49.15, e2022GL098616. DOI: 10.1029/2022GL098616.

Whaler, K. A., N. Olsen, and C. C. Finlay (2016). Decadal variability in core surface flows deduced from geomagnetic observatory monthly means. *Geophys. J. Int.* 207.1, 228–243. DOI: 10.1093/gji/ggw268.

Wu, K., X. Song, and Y. Yang (2026). Pattern of Inner-Core Differential Rotation From Long-Term Earthquake Sequences and USArray Network. *Geophys. Res. Lett.* 53.1. DOI: 10.1029/2025GL119295.

Yang, Y. and X. Song (2023). Multidecadal variation of the Earth's inner-core rotation. *Nat. Geosci.* 16.2, 182–187. DOI: 10.1038/s41561-022-01112-z.